Direct measurement of emittance in the Muon Ionization Cooling Experiment

V. Blackmore, C. Hunt, K. Long

The Muon Ionization Cooling Experiment (MICE) collaboration seeks to demonstrate the feasibility of ionization cooling, the technique by which it is proposed to cool the muon beam at a future neutrino factory or muon collider. The emittance is derived from an ensemble of muons assembled from those that pass through the experiment. A pure muon ensemble is selected using a particle identification system that can reject efficiently both pions and electrons. The position and momentum of each muon is measured using a high-precision scintillating-fibre tracker in a 4 T solenoidal magnetic field. This paper presents the techniques used to reconstruct the phase-space distributions and reports the emittance of the muon beam as a function of muon-beam momentum.

1 Introduction

Stored muon beams have been proposed as the source of neutrinos at a neutrino factory [1, 2] and as the means to deliver multi-TeV lepton-antilepton collisions at a muon collider [3, 4]. In such facilities the muon beam is produced from the decay of pions generated by a high-power proton beam striking a target. The tertiary muon beam occupies a large volume in phase space. To optimise the muon yield for a neutrino factory, and luminosity for a muon collider, while maintaining a suitably small aperture in the muon-acceleration system requires that the muon beam be "cooled" (i.e., its phase-space volume reduced) prior to acceleration[1].

A muon is short-lived, with a lifetime of 2.2 μs in its rest frame. Therefore, beam manipulation at low energy (≤ 1 GeV) must be carried out rapidly. Four cooling techniques are in use at particle accelerators: synchrotron-radiation cooling [6]; laser cooling [7–9]; stochastic cooling [10]; and electron cooling [11]. In each case, the time taken to cool the beam is long compared to the muon lifetime. In contrast, ionization cooling is a process that occurs on a short timescale. A muon beam passes through a material (the absorber), loses energy, and is then reaccelerated, cooling the beam efficiently with modest decay losses. Ionization cooling is therefore the technique by which it is proposed to increase the number of particles within the downstream acceptance, for a neutrino factory, and phase-space density for a muon collider [12–14]. This technique has never been demonstrated experimentally and such a demonstration is essential for the development of future high-brightness muon accelerators.

The international Muon Ionization Cooling Experiment (MICE) has been designed [15] to perform a full demonstration of transverse ionization cooling. Intensity effects are negligible for most of the cooling channels conceived for the neutrino factory or muon collider [16]. This allows the MICE experiment to record muon trajectories one particle at a time. The MICE collaboration has constructed two solenoidal spectrometers, one placed upstream, the other downstream, of the cooling cell. An ensemble of muon trajectories is assembled offline, selecting an initial distribution based on quantities measured in the upstream particle identification detectors and upstream spectrometer. This paper describes the techniques used to reconstruct the phase-space distributions in the spectrometers and presents a measurement of the emittance of a variety of momentum-selected muon ensembles.

[1] A recent paper [5] describes an alternative method of producing a low emittance muon beam, by production of $\mu^+\mu^-$ pairs close to threshold; but there remain unsolved problems before this can be used to produce a beam suitable for muon collider or neutrino factory.

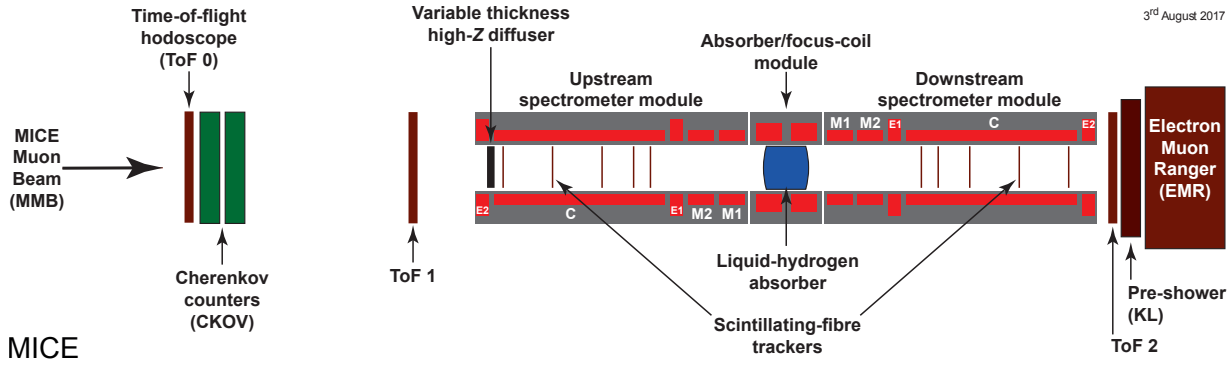

Figure 1: Schematic diagram of the configuration of the experiment. The red rectangles represent the coils of the spectrometer solenoids and focus coil. The individual coils of the spectrometer solenoids are labelled E1, C, E2, M1 and M2. The various detectors (time-of-flight hodoscopes [18, 19], Cerenkov counters [20], scintillating-fibre trackers [21], KLOE Light (KL) calorimeter [22, 23], electron muon ranger [24]) used to characterise the beam are also represented.

2 Calculation of emittance

Emittance is a key parameter in assessing the overall performance of an accelerator [17]. The luminosity achieved by a collider is inversely proportional to the colliding beam's emittance, and therefore beams with small emittance are required.

A beam travelling through a portion of an accelerator may be described as an ensemble of particles. Consider a beam that propagates in the positive z direction of a right-handed Cartesian coordinate system, (x, y, z). The position of the i^{th} particle in the ensemble, $\mathbf{r}_i = (x_i, y_i)$, and its transverse momentum, $\mathbf{p}_i = (p_{xi}, p_{yi})$, then define the coordinates of the particle in transverse phase space. The normalised transverse emittance, ε_N, of the ensemble approximates the volume occupied by the particles in four-dimensional phase space and is given by:

$$\varepsilon_N = \frac{1}{m_\mu} \sqrt[4]{\det \mathcal{C}}\,; \tag{1}$$

where m_μ is the rest mass of the muon, $\mathcal{C}$ is the four-dimensional covariance matrix defined by:

$$\mathcal{C} = \begin{pmatrix} \sigma_{xx} & \sigma_{xp_x} & \sigma_{xy} & \sigma_{xp_y} \\ \sigma_{xp_x} & \sigma_{p_xp_x} & \sigma_{yp_x} & \sigma_{p_xp_y} \\ \sigma_{xy} & \sigma_{yp_x} & \sigma_{yy} & \sigma_{yp_y} \\ \sigma_{xp_y} & \sigma_{p_xp_y} & \sigma_{yp_y} & \sigma_{p_yp_y} \end{pmatrix}\,; \tag{2}$$

and

$$\sigma_{\alpha\beta} = \frac{1}{N-1}\left(\Sigma_i^N \alpha_i\beta_i - \frac{\left(\Sigma_i^N \alpha_i\right)\left(\Sigma_i^N \beta_i\right)}{N}\right)\,. \tag{3}$$

The MICE experiment is operated such that muons pass through the experiment one at a time. The phase-space coordinates of each muon are measured. An ensemble of muons that is representative of the muon beam is assembled using the measured coordinates. The normalised transverse emittance of the ensemble is then calculated by evaluating the sums necessary to construct the covariance matrix, $\mathcal{C}$, and using equation 1.

3 The Muon Ionization Cooling Experiment

The muons for MICE come from the decay of pions produced by an internal target dipping directly into the circulating proton beam in the ISIS synchrotron at the Rutherford Appleton Laboratory (RAL) [25, 26]. The burst of particles resulting from one target dip is referred to as a 'spill'. A transfer line of nine quadrupoles, two dipoles and a superconducting 'decay solenoid' selects a momentum bite and transports the beam into the experiment [22] (the MICE Muon Beam). The small fraction of pions that remain in the beam are rejected during analysis using the time-of-flight hodoscopes and Cherenkov counters that are installed in the MICE Muon Beam upstream of the cooling channel [27]. A diffuser is installed at the upstream end of the experiment to vary the initial emittance of the beam [22]. The diffuser introduces a variable amount of high-Z material into the beam path, varying the input beam emittance that is transported to the absorber.

A schematic diagram of the experiment is shown in figure 1. It contains an absorber/focus-coil module sandwiched between two spectrometer-solenoid modules that provide a uniform magnetic field for particle measurement. The focus-coil module has two separate windings that can be operated with the same, or opposed, polarity. A lithium-hydride or liquid-hydrogen absorber can be placed at the centre of the focus-coil module.

The emittance is measured upstream and downstream of the absorber and focus-coil using scintillating-fibre tracking detectors [21] immersed in the solenoidal field provided by three superconducting coils (E1, C, E2). The trackers are used to reconstruct the trajectories of individual muons at the entrance and exit of the absorber. The trackers are each constructed from 5 planar stations of scintillating fibres. The track parameters are reported at the nominal reference plane; the surface of the scintillating-fibre plane closest to the absorber/focus-coil module [28]. The reconstructed tracks are combined with information from instrumentation upstream and downstream of the spectrometer modules to measure the muon-beam emittance at the upstream and downstream tracker reference planes. The instrumentation up- and downstream of the spectrometer modules is used to select a pure sample of muons. The spectrometer-solenoid modules also contain two superconducting "matching" coils (M1, M2) that are used to match the optics between the solenoid field region and the neighbouring focus-coil.

4 MICE Muon Beam line

The MICE Muon Beam line (MMB), shown schematically in figure 2, is capable of delivering beams with normalised transverse emittance in the range $3 \leq \varepsilon_N \leq 10\pi$ mm and mean momentum in the range $140 \leq p_\mu \leq 240$ MeV/c with a root-mean-squared (RMS) momentum spread of $\sim$20 MeV/c [22] after a "diffuser" (figure 1). The pneumatically operated diffuser, consisting of tungsten and brass irises of various thickness, is at the entrance to the upstream spectrometer module to generate the required range of emittance.

Pions produced by the momentary insertion of a titanium target [25, 26] into the ISIS proton beam are captured using a quadrupole triplet (Q1–3) and transported to a first dipole magnet (D1), which selects particles of a desired momentum bite into the 5 T decay solenoid (DS). Muons produced in pion decay in the DS are momentum-selected using a second dipole magnet (D2) and focused onto the diffuser by a quadrupole channel (Q4–6 and Q7–9). In positive-beam running, a borated polyethylene absorber of variable thickness is inserted into the beam just downstream of the decay solenoid to suppress the high rate of protons that are produced at the target [29].

The composition and momentum spectra of the beams delivered to MICE are determined by the interplay between the two bending magnets D1 and D2. In "muon" mode, D2 is set to half the current of D1, selecting backward-going muons in the pion rest frame and producing an almost pure muon beam.

Data were taken in October 2015 in muon mode at a nominal momentum of 200 MeV/c, with ISIS in operation at 700 MeV. These measured muons are used here to characterise the properties of the beam accepted

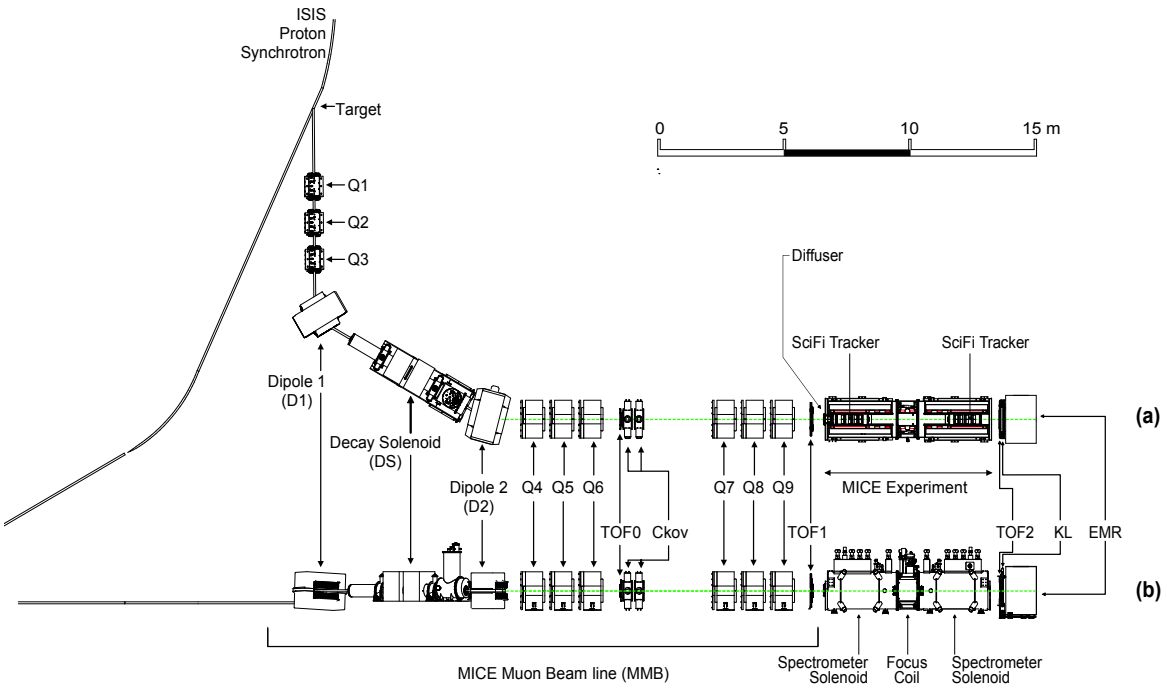

Figure 2: (a) Top and (b) side views of the MICE Muon Beam line, its instrumentation, and the experimental configuration. A titanium target dips into the ISIS Proton Synchrotron and the resultant spill of particles is captured with a quadrupole triplet (Q1–3) and transported through momentum-selecting dipoles (D1, D2). The final quadrupole triplets (Q4–6, Q7–9) transport particles to the upstream spectrometer module. The time-of-flight of particles, measured between TOF0 and TOF1, is used for particle identification.

by the upstream solenoid with all diffuser irises withdrawn from the beam. The upstream E1-C-E2 coils in the spectrometer module were energised and produced a 4 T field, effectively uniform across the tracking region, while all other coils were unpowered.

5 Simulation

Monte Carlo simulations were used to determine the accuracy of the kinematic reconstruction, to evaluate the efficiency of the response of the scintillating-fibre tracker, and to study systematic uncertainties. A sufficient number of events were generated to ensure that statistical uncertainties from the simulations were negligible in comparison to those of the data.

The beam impinging on TOF0 was produced using G4beamline [30]. Particles were produced at the target using a parameterised production model assuming 800 MeV operation of the ISIS proton synchrotron. These particles were tracked through the MICE Muon Beam line taking into account all material in and surrounding the beam line and using realistic models of the field and apertures of the various magnets. The G4beamline-simulation was tuned to reproduce the observed particle distributions at TOF0.

The MICE User Analysis Software (MAUS) [31] package was used to simulate the passage of particles from TOF0 through the remainder of the MICE Muon Beam to the solenoidal lattice. This simulation includes the response of the instrumentation, and used the input distribution produced using G4beamline. In addition to simulation, MAUS also provides a framework for data analysis. MAUS is used for offline analysis and to provide fast real-time detector reconstruction and data visualisation during MICE running. MAUS uses GEANT4 [32, 33] for beam propagation and the simulation of detector response. The events generated were

subjected to the same trigger requirements as the data and processed by the same reconstruction programs. ROOT [34] is used for data visualisation and for data storage.

5.1 Simulated distributions

The MAUS simulation provides a good description of the measured particle distributions (see Section 6), but does not precisely replicate the measured data.

- *Input distribution:* The production of particles on the titanium target that dips into the ISIS proton beam is parameterised. The position distributions transported to the TOF0 detector by G4Beamline are in coarse agreement with the position-distributions measured at TOF0. Similarly, the time-of-flight distribution of the simulated particles differs from the measured time-of-flight (see Section 6).
- *Accuracy of magnetic field models:* The magnetic field used to reconstruct particles in the Monte Carlo assumes the cold, as-built, dimensions of coils in the upstream Spectrometer Solenoid. The magnetic field produced by these coils is calculated using a COMSOL [35] model that includes the iron Partial Return Yoke. Improving the accuracy of the field model will reduce the systematic error on the measurement (see Section 8.2).

The inconsistency between reconstructed data and reconstructed simulation does not affect the calculation of normalised transverse emittance, as the measurement of the position and momentum of individual particles does not depend on the Monte Carlo simulation.

6 Beam selection

The experiment is read out at the end of each spill. This makes it necessary to buffer digital information related to the passage of the particles through the experiment in the front-end electronics (for a description of the MICE trigger and data-acquisition system see [22]). For the reconstructed data presented here, the digitisation of the analogue signals received from the detectors was triggered by a coincidence of signals in the two PMTs serving a single scintillator slab in TOF1. Any slab in TOF1 could generate a trigger.

The following cuts were used to select muons passing through the upstream tracker:

- *One reconstructed space-point in TOF0 and TOF1*: Each TOF hodoscope is composed of two perpendicular planes of scintillator slabs arranged to measure the x and y coordinates. A space-point is formed from the intersection of hits in the x and y projections. Figure 3 shows the hit multiplicity in TOF0 plotted against the hit multiplicity in TOF1. The sample is dominated by events with one space-point in both TOF0 and TOF1. This cut removes events in which two particles enter the experiment within the trigger window;
- *Relative time-of-flight between TOF0 and TOF1,* t_{n01}*, in the range* $1 \leq t_{n01} \leq 6\,ns$: Figure 3 shows the relative time-of-flight distribution, where both data and Monte Carlo distributions have been normalised to the same mean electron time-of-flight, t_e. All cuts other than the time-of-flight cut have been applied in this figure. The calibrated time-of-flight of a particle depends on the time taken to pass between TOF0 and TOF1, t_{01} and the path length travelled by an electron, $(L + s)$, in the field of the quadrupole triplet, where s is the excess distance over the longitudinal separation between TOF0 and TOF1, L [27]. The nominal distance between TOF0 and TOF1 is 7.78 m, and the time-of-flight of particles relative to the electron time is calculated as:

$$t_{n01} = t_{01} - t_e + \frac{L + s}{c}\,.$$

  This cut removes electrons from the selected ensemble as well as a small number of pions.

- *A single track reconstructed in the upstream tracker with a track-fit χ^2 satisfying $\frac{\chi^2}{N_{\rm DOF}} \leq 4$:* $N_{\rm DOF}$ is the number of degrees of freedom. The distribution of $\frac{\chi^2}{N_{\rm DOF}}$ is shown in figure 3. The disagreement between reconstructed data and reconstructed simulation is due to differences in the assumed material of the Tracker used in the simulation. The disagreement shown here does not affect particle selection, as the criteria on this parameter is such that both distributions are well-contained beneath the chosen value of $\frac{\chi^2}{N_{\rm DOF}} \leq 4$. This cut removes events with poorly reconstructed tracks. Multi-track events, where more than one particle passes through the same pixel in TOF0 and TOF1 during the trigger window, are rare but are also removed by this cut.

- *Track contained within the fiducial volume of the tracker*: The radius of the track at each tracker station, $R_{\rm stn}$, is required to satisfy $R_{\rm stn} < 150\,$mm. To ensure the track does not leave and then re-enter the fiducial volume, the track radius is evaluated at 1 mm intervals between the stations. If the track radius exceeds 150 mm at any of these positions, the event is rejected;

- *Track radius at the diffuser, $R_{\rm diff} \leq 90\,mm$*: Muons that pass through the material of the diffuser, which includes the retracted irises, lose a substantial amount of energy. Such muons may re-enter the tracking volume and be reconstructed but have properties that are no longer characteristic of the incident muon beam. The inner radius of the diffuser mechanism (100 mm) defines the transverse acceptance of the beam injected into the experiment. Back-extrapolation of tracks to the exit of the diffuser yields a measurement of $R_{\rm diff}$ with a resolution of $\sigma_{R_{\rm diff}} = 1.7\,$mm. Figure 3 shows the distribution of $R_{\rm diff}$. The cut on $R_{\rm diff}$ accepts particles that passed within $5.9\sigma_{R_{\rm diff}}$ of the inner radius of the diffuser; and

- *Particle consistent with muon hypothesis:* Figure 4 shows t_{01}, the time-of-flight between TOF0 and TOF1, plotted as a function of p, the momentum reconstructed by the upstream tracking detector. The same distribution obtained from the simulation is also shown. The time-of-flight of a muon that loses the mean momentum measured between TOF1 and the upstream tracking detector, $\Delta p \simeq 20\,$MeV/c, is also shown. Muons are accepted into the sample if the measured time-of-flight (t_{01}) is consistent with that expected, based on the measured muon momentum ($p_{\rm Tk}$). To be accepted the difference between the momentum inferred from t_{01}, $p_{\rm TOF}$, must satisfy $|p_{\rm TOF} - p_{\rm Tk}| < 22\,$MeVc. Events for which $p_{\rm TOF} - p_{\rm Tk} > 22\,$MeV/c are ascribed to the passage of pions, or mis-reconstructed muons, and are removed from the analysis. The population of events for which $p_{\rm TOF} - p_{\rm Tk} < -22$ arise from muons that are poorly reconstructed or have passed through support material upstream of the tracker and lost significant momentum. These muons are also removed from the analysis. 19 155 events are removed by this requirement.

A total of 24 660 events pass the cuts listed above. Table 1 shows the number of particles that survive each individual cut. Data distributions are compared to the distributions obtained using the MAUS simulation in figure 3. The distribution of the time of flight between TOF0 and TOF1 is peaked towards slightly longer times in the simulation than in the data. This is related to the imperfect simulation of the distribution of longitudinal momentum of particles in the beam (see below). The distribution of $\frac{\chi^2}{N_{\rm DOF}}$ is broader and peaked at slightly larger values in the data than in the simulation. Despite these minor disagreements, the agreement between the simulation and data is sufficiently good to give confidence that a clean sample of muons has been selected.

Table 2 shows the proportions of positrons, muons, and pions in the MAUS simulation that pass all selection criteria. The expected pion contamination in the unselected ensemble of particles is 0.4% [36]. The criteria used to select the muon sample for the analysis presented here efficiently rejects electrons and pions from the Monte Carlo sample.

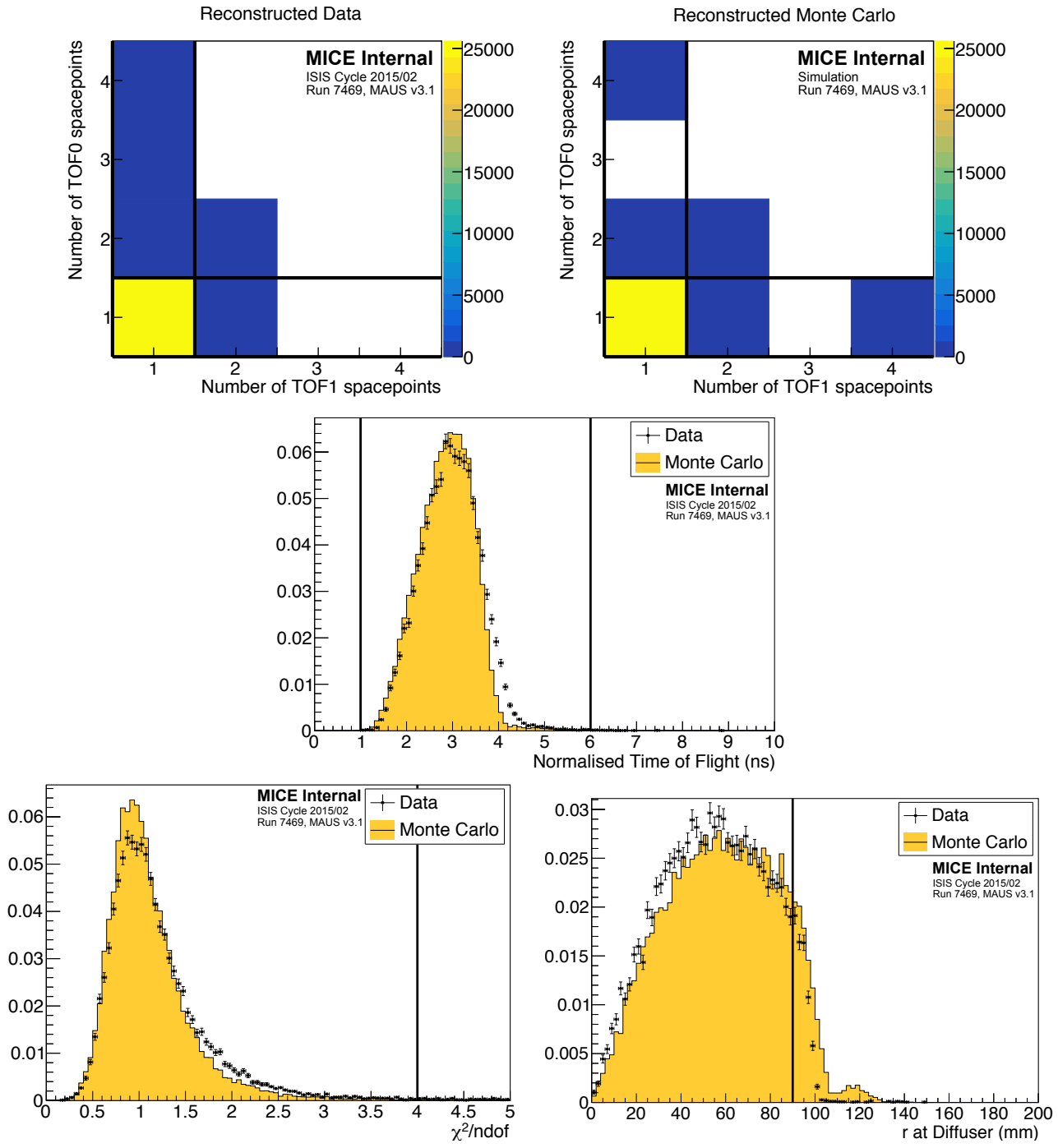

Figure 3: Distribution of the quantities that select the sample used to reconstruct the emittance of the beam. Top: the number of space-points in TOF0 plotted against the number of space-points in TOF1 (left) reconstructed data, (right) reconstructed simulation; Middle: distribution of the normalised time-of-flight, t_{n01}; Bottom left: distribution of $\frac{\chi^2}{N_{\rm DOF}}$; and Bottom right: distribution of $R_{\rm diff}$. The 1D distributions show reconstructed data as solid (black) circles and reconstructed MAUS simulation as the solid (yellow) histogram. The solid (black) lines indicate the position of the cuts made on these quantities. Events enter these plots if all cuts other than the cut under examination are passed.

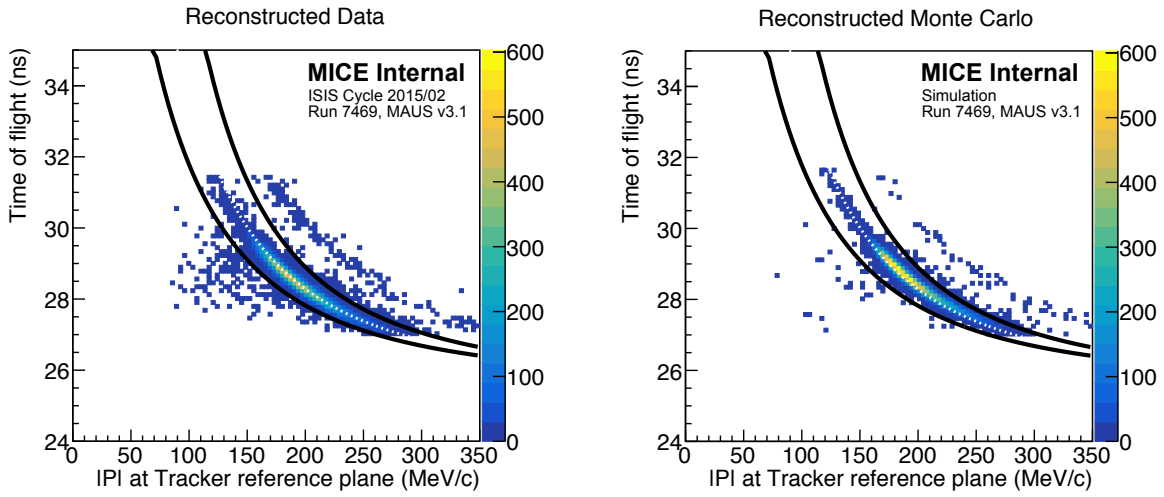

Figure 4: Time of flight between TOF0 and TOF1 (t_{01}) plotted as a function of the muon momentum, p, measured in the upstream tracker. All cuts other than the muon hypothesis have been applied. Particles within the black lines are selected as a pure muon sample. The (white) dotted line is the trajectory of a muon that loses the mean momentum (20 MeV/c) between TOF1 and the tracker. (Left) Reconstructed Data, (Right) Reconstructed Monte Carlo.

Table 1: The number of particles that pass each selection criteria in isolation. A total of 24 660 particles pass all of the described cuts.

Cut	No. surviving particles	Cumulative surviving particles
None	53 276	53 276
One space-point in TOF0 and TOF1	37 619	37 619
Time of flight in range 27—32 ns	37 093	36 658
Single reconstructed track with $\frac{\chi^2}{N_{\mathrm{DOF}}} \leq 4$	40 110	30 132
Track within fiducial volume of tracker	52 039	29 714
Tracked radius at diffuser $\leq$ 90 mm	42 593	25 310
Muon hypothesis	34 121	24 660
All	24 660	24 660

Table 2: The proportion of electrons, muons, and pions at the upstream Tracker that survive each cut in the Monte Carlo simulation. Application of all cuts removes all but one electron and pion in the reconstructed Monte Carlo sample. A total of 25 600 particles pass all of the described cuts in the Monte Carlo simulation.

Cut	e	μ	π	Total
None	1 611	44 424	190	47 674
One space-point in TOF0 and TOF1	1224	36 317	147	38 699
Time of flight in range 27—32 ns	55	37 888	148	38 926
Single reconstructed track with $\frac{\chi^2}{N_{\mathrm{DOF}}} \leq 4$	1 197	42 486	162	43 848
Track within fiducial volume of tracker	1 581	42 458	172	44 211
Tracked radius at diffuser $\leq$ 90 mm	1 304	31 200	107	32 611
Muon hypothesis (above lower limit)	345	37 398	152	37 895
Muon hypothesis (below upper limit)	1424	42 263	39	44 106
Muon hypothesis (overall)	297	37 054	37	37 390
All	1	25 598	1	25 600

7 Results

7.1 Phase-space projections

The distributions of $x, y, p_x, p_y, p_z, p_\perp^2, p_\perp$ (where $p_\perp^2 = p_x^2 + p_y^2$), and $p = \sqrt{p_x^2 + p_y^2 + p_z^2}$ are shown in figure 5. The total momentum of the muons that make up the beam lie within the range $140 \lesssim |p| \lesssim 260$ MeV/c. The results of the MAUS simulation, which are also shown in figure 5, give a reasonable description of the data. In the case of the longitudinal component of momentum, p_z, the data is peaked to slightly larger values than the simulation. The difference is small and is reflected in the distribution of the total momentum, p. The distributions of the components of the transverse phase space (x, p_x, y, p_y) are well described by the simulation, with the exception of a deviation in the position of the beam in the y direction that persists across the tracking volume. This effect is also small and has a negligible effect on the reconstruction of emittance.

The phase space occupied by the selected beam is shown in figure 6. The distributions are plotted at the reference surface of the upstream tracker. The beam is moderately well centred in the (x, y) plane. Correlations are apparent that couple the position and momentum components in the transverse plane. The transverse position and momentum coordinates are also seen to be correlated with total momentum. The dispersion and chromaticity of the beam is discussed further in section 7.2.

7.2 Dispersion, chromaticity, and binning in longitudinal momentum

Momentum selection at D2 introduces a correlation between position and momentum. Figure 7 shows the transverse positions and momenta with respect to the momentum, p, as measured at the upstream tracker reference plane. Correlations exist between all four transverse phase-space co-ordinates and the longitudinal momentum.

The momentum-dependence of the orientation of the phase-space projections, or chromaticity, is demonstrated in figure 8. The ensemble shown in figure 8 is divided into 10 MeV/c bins of total momentum, p. As p increases, the phase space volume occupied by the beam rotates. If the emittance of the selected ensemble was calculated for all momenta, the apparent phase space volume of the ensemble would increase due to the

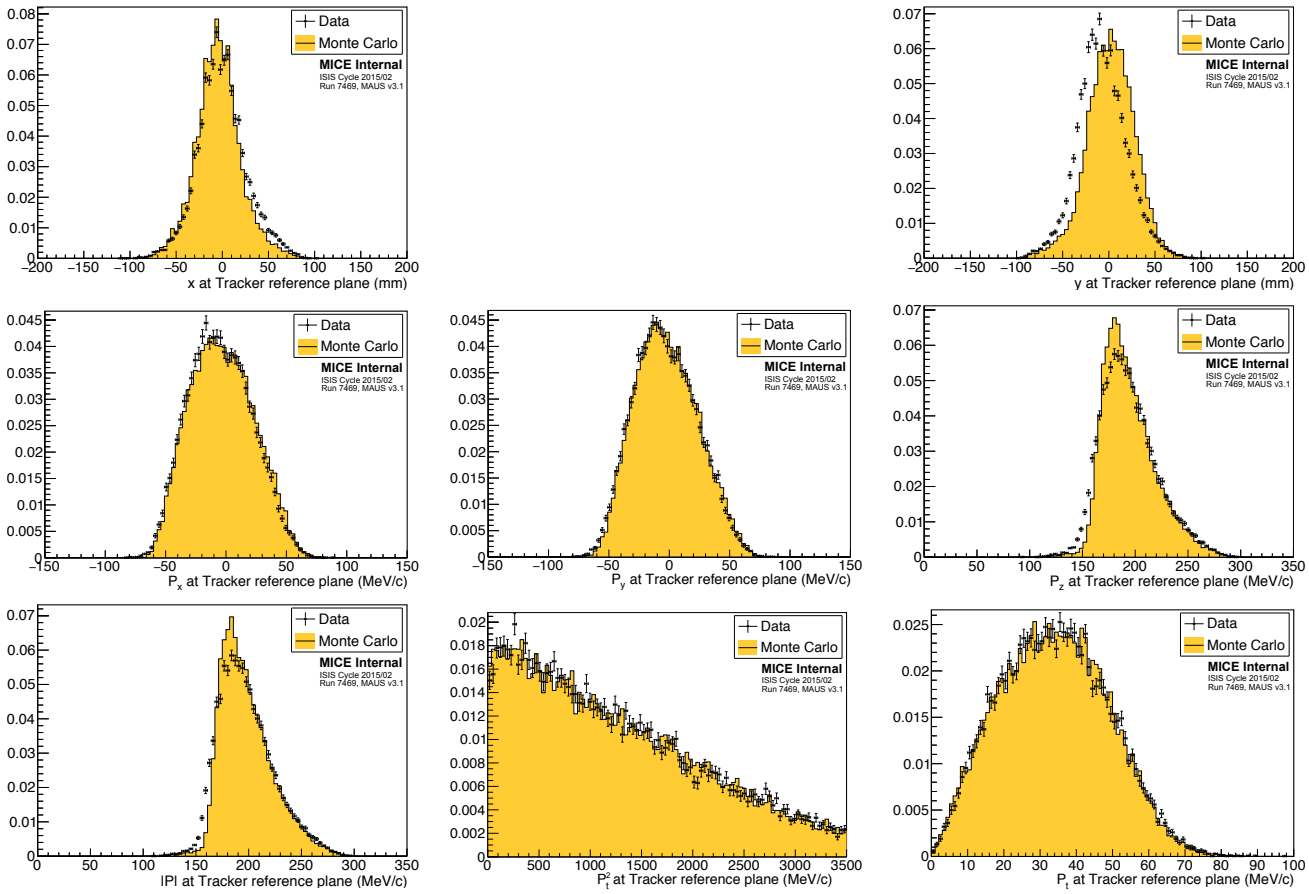

Figure 5: Position and momentum distributions of muons reconstructed at the reference surface of the upstream tracker. The top left and top right panels show the distributions of x and y respectively. The distributions of components of the muon momentum are shown in the middle row; p_x in the left-middle panel, p_y in the centre middle panel and p_z in the right-middle panel. The distribution of the total momentum, p, is shown in the bottom-left panel. The distributions of the transverse momentum squared, $p_\perp^2 = p_x^2 + p_y^2$, and $p_\perp$ are shown in the bottom-middle and bottom-right panels respectively. The data is shown as the solid circles while the results of the MAUS simulation are shown as the yellow histogram.

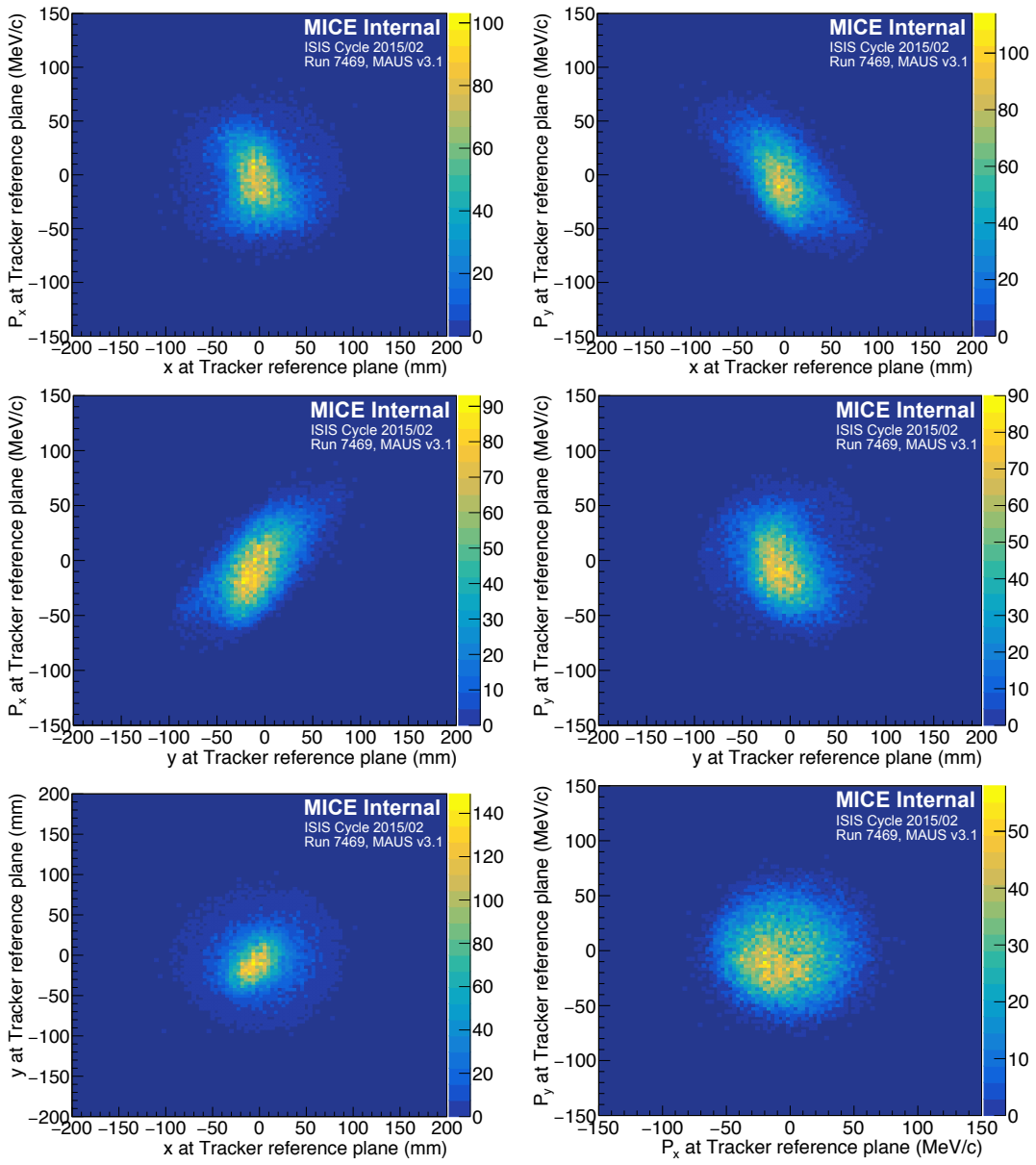

Figure 6: Transverse phase space occupied by selected muons transported through the MICE Muon Beam to the reference plane of the upstream Tracker. Top left: (x, p_x), top right: (x, p_y). Middle left: (y, p_x), middle right: (y, p_y). Bottom left: (x, y), bottom right: (p_x, p_y).

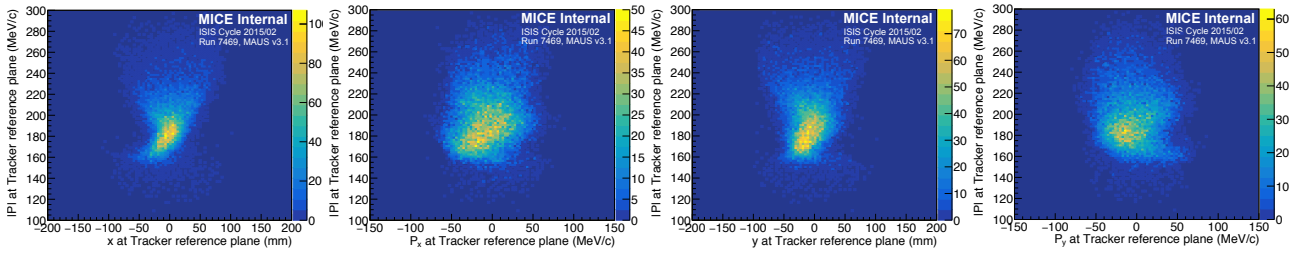

Figure 7: Dispersion is shown, from left to right, in x, p_x, y, and p_y, with respect to the longitudinal momentum, p, measured at the upstream Tracker reference plane.

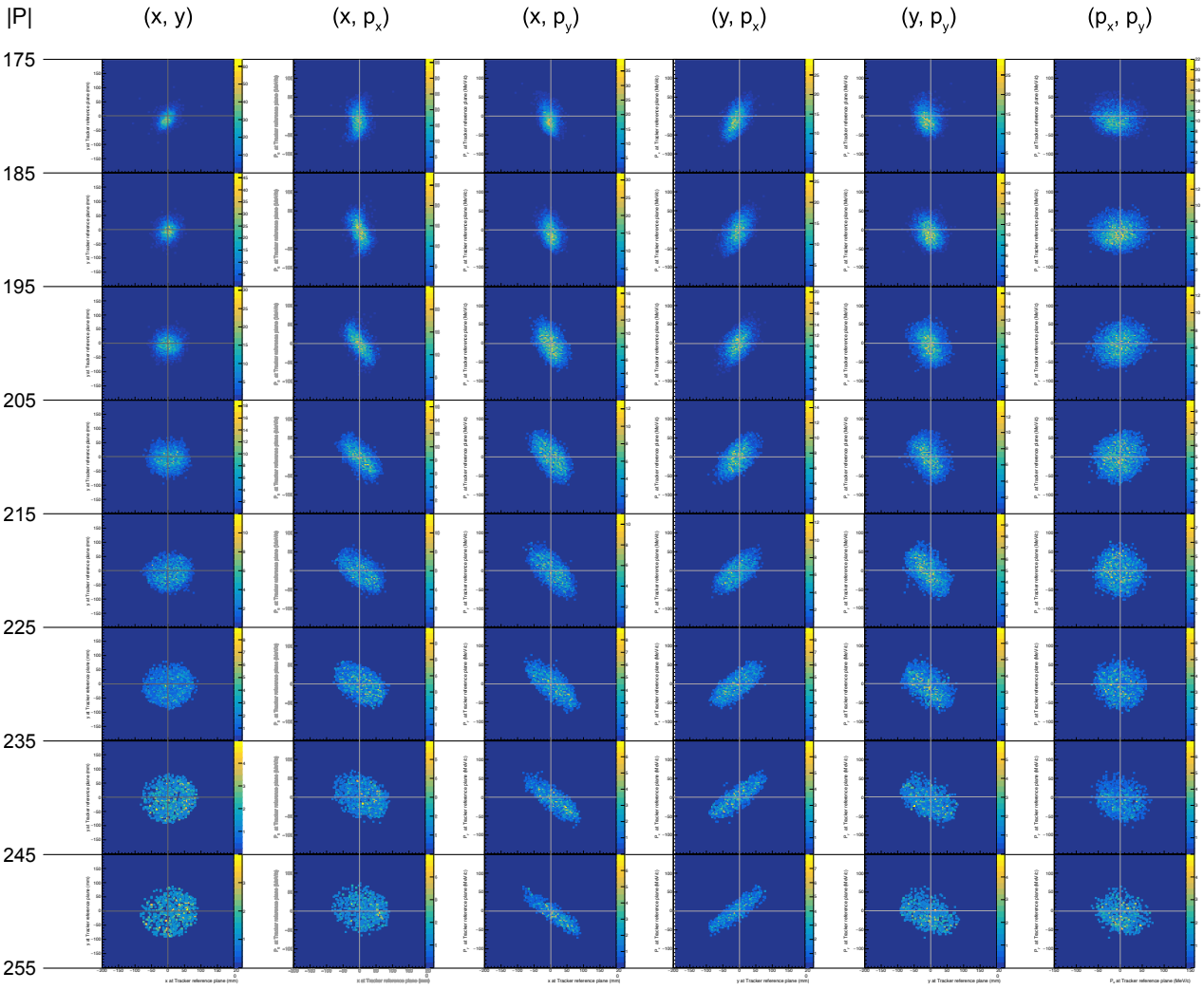

Figure 8: Phase-space distributions binned in 10 MeV/c increments of total momentum, p. The orientation of the phase-space projections is momentum-dependent. The axis arrangement and scale of each phase-space projection are as in the equivalent figure showing particles of all momenta, figure 6.

optical mismatch. To compensate for this, the ensemble is divided into 10 MeV/c momentum (p) bins, and the transverse normalised emittance is calculated for each individual bin.

Figure 9 shows the transverse position of muons tracked to the downstream face of the diffuser in the 10 MeV/c momentum bins. A subset of the beam selection cuts were used for this figure alone: only muons that survive the criteria on normalised time-of-flight, $\frac{\chi^2}{N_{\mathrm{DOF}}}$, and that are fully contained within the tracking detector are shown. The diffuser has an aperture of 100 mm, which is shown by the white (dotted) circles. Particles that fall outside an aperture of 90 mm are removed from the analysis (Section 6). As p increases the ensemble moves onto the design momentum of the MICE Muon Beam ($p \simeq 200$ MeV/c). At momenta less than 185 MeV/c, the majority of the particles are scraped from the beam by various apertures along the beamline. The low momentum region is therefore removed from the analysis and the reported emittance is calculated in 10 MeV/c bins, beginning at $p = 185$ MeV/c.

The size of the bins in p used to report the calculated emittance were chosen commensurate with the resolution. The p resolution, σ_p, plotted as a function of p in figure 10, increases approximately linearly from ~ 1.1 MeV/c at 175 MeV/c to ~ 2.3 MeV/c at 255 MeV/c. A bin width of 10 MeV/c was therefore chosen.

The number of events per bin is shown in figure 11. The number of events per bin varies from $\sim$ 4 000 for $p \sim 190$ MeV/c to $\sim$ 700 for $p \sim 250$ MeV/c. The binning-efficiency, η, and purity, ζ, were evaluated using Monte Carlo to quantify the small amount of migration between neighbouring momentum bins. For each momentum bin, the number of particles generated with true p in the bin, N_G, is counted as well as the number of particles with a reconstructed p in the bin, N_R. Particles with both true and reconstructed momentum in the bin that also satisfy the selection criteria discussed in Section 6, are counted as N_c. The binning-efficiency and purity are then defined as:

$$\eta = \frac{N_c}{N_G}\,; \text{and} \tag{4}$$

$$\zeta = \frac{N_c}{N_R}\,. \tag{5}$$

The binning efficiency and purity are always ≈ 1 (see figure 11 where $1-\eta$ and $1-\zeta$ are plotted as a function of momentum).

8 Uncertainties on emittance measurement

8.1 Statistical uncertainties

The statistical uncertainty on the emittance of each momentum bin is calculated as $\sigma_\varepsilon = \frac{\varepsilon}{\sqrt{2N}}$ [37–39], where ε is the emittance of the ensemble of muons in the specified momentum range and N is the number of muons in that ensemble. The number of events per bin is shown in figure 11.

8.2 Systematic uncertainties

Systematic uncertainties related to the beam selection were estimated by varying the cut values by an amount corresponding to the RMS resolution of the quantity in question. Systematic uncertainties related to possible biases in calibration constants were evaluated by varying each calibration constant in line with its resolution. Systematic uncertainties related to the reconstruction algorithms were evaluated using the MAUS simulation. The positive and negative deviations from the nominal emittance were added in quadrature separately to obtain the total positive and negative systematic uncertainly. Sources of uncorrelated and correlated uncertainties are discussed in detail below.

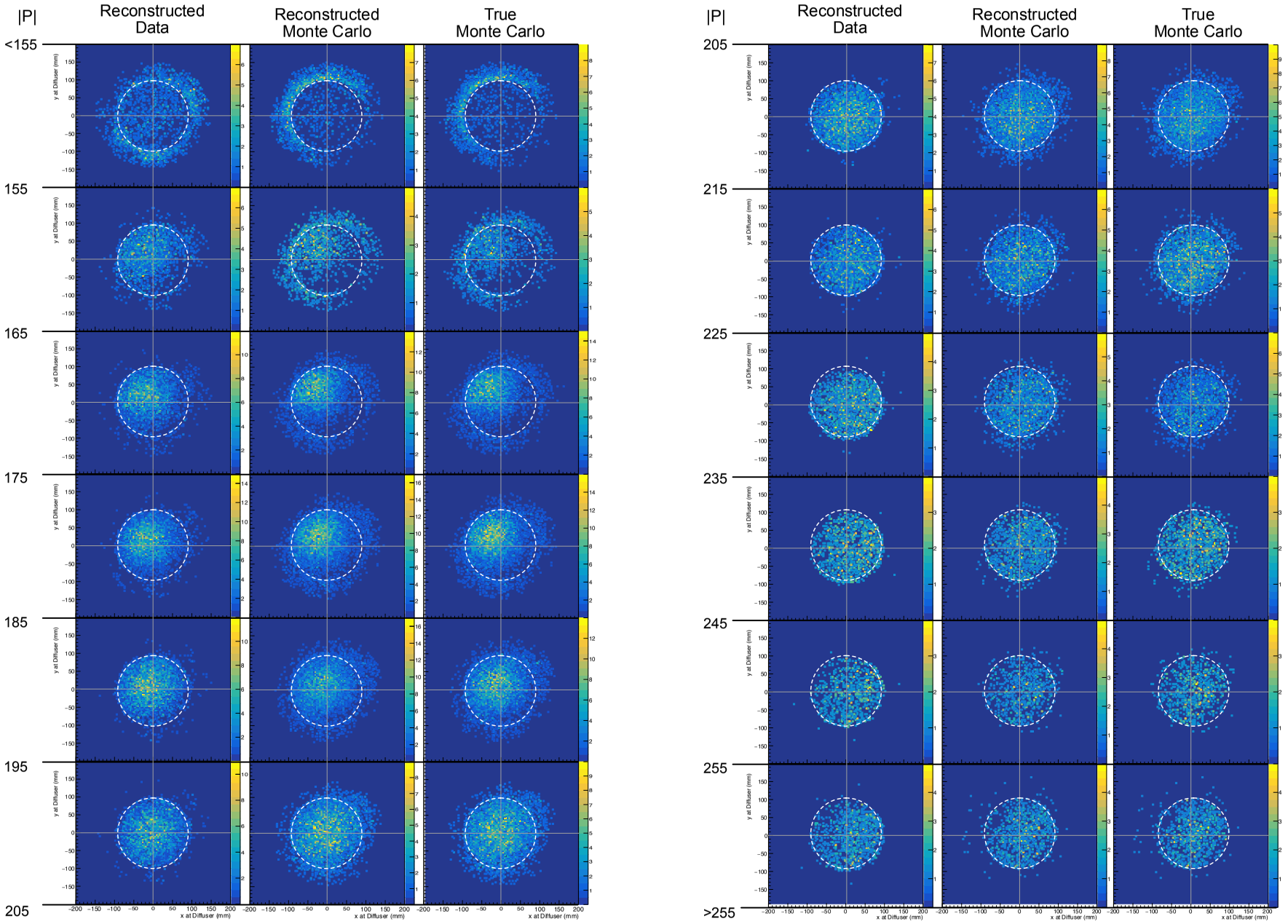

Figure 9: Particle position tracked to the downstream face of the diffuser, in 10 MeV/c increments of total momentum, p, measured at the reference surface of the upstream tracking detector. Each increment of p shows (left) reconstructed and tracked data, (middle) reconstructed and tracked simulation, and (right) true simulated particle position. This figure shows particles that pass the selection criteria on normalised time-of-flight, and a single track with $\frac{\chi^2}{N_{\mathrm{DOF}}} \leq 4$ that is fully contained within the tracker. Particles at a radius greater than 90 mm in this figure are removed by additional selection criteria. The diffuser aperture of 100 mm is shown by the white (dashed) circle. (section 6).

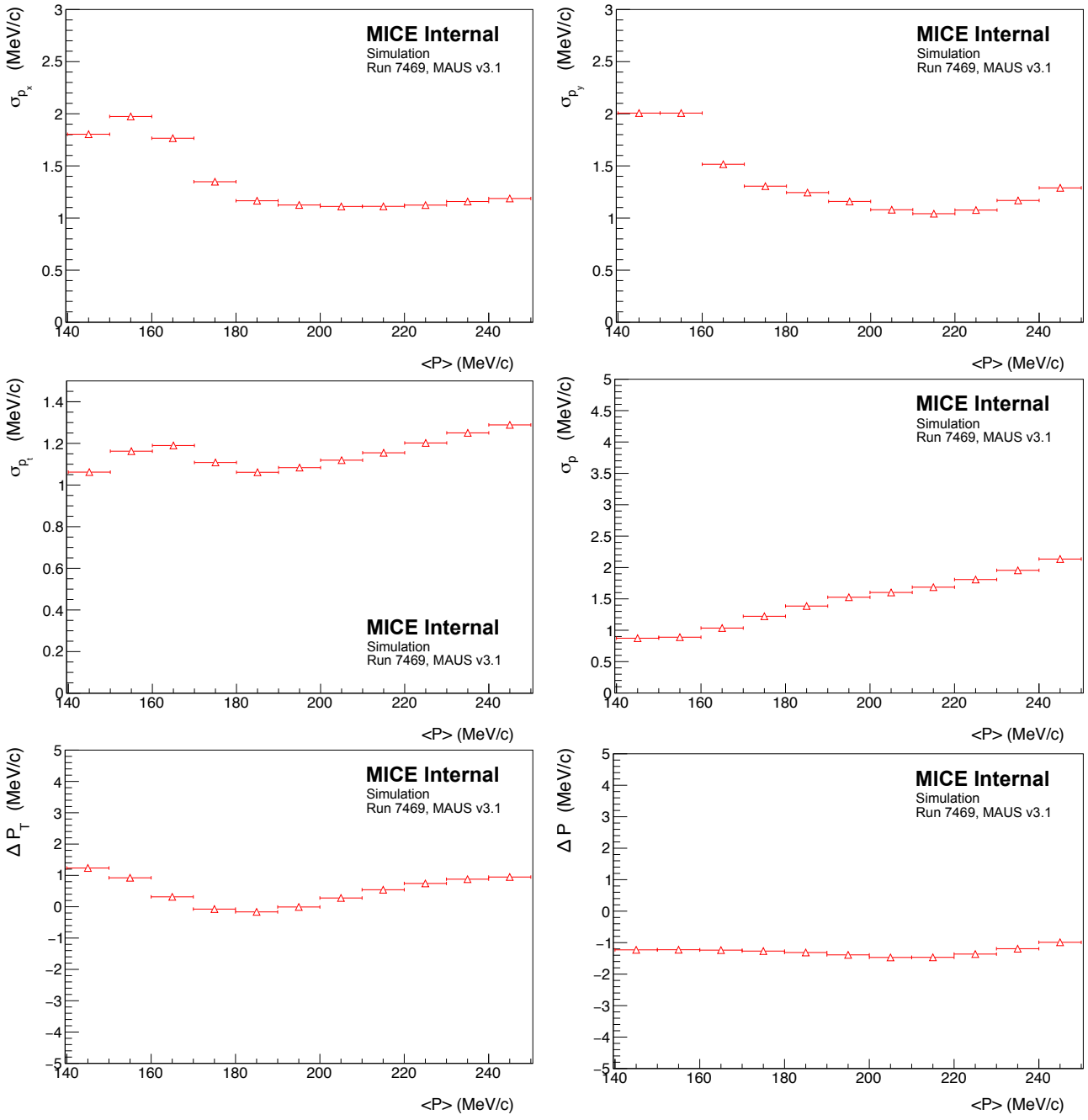

Figure 10: Resolution and bias of reconstructed track parameters as a function of p at the upstream tracker reference plane. Top left: Reconstruction resolution on p_x, top right: p_y, middle left: $p_\perp$, middle right: p. Bottom left: Reconstruction bias on $p_\perp$, bottom right: p.

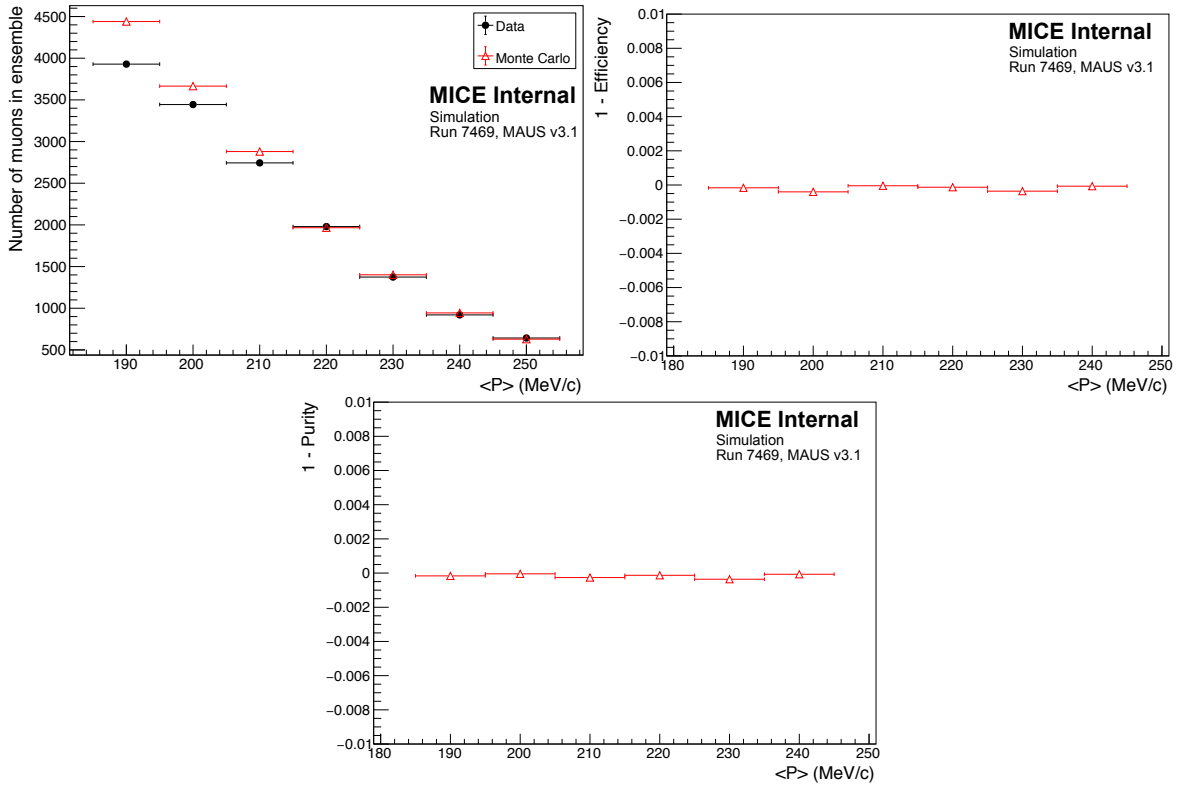

Figure 11: Top left: The number of muons in each momentum bin in reconstructed data (black, circle) and reconstructed Monte Carlo (red, triangle). Top right: $1 - \eta$, where η is the reconstructed Monte Carlo selection binning-efficiency, as a function of p. Bottom: $1 - \zeta$, where ζ is the reconstructed Monte Carlo selection binning-purity, as a function of p. Both efficiency and purity are ≈ 1.

8.2.1 Uncorrelated systematic uncertainties

Systematic uncertainties related to beam selection have been estimated by varying the cut values according to the RMS resolution of the cut variables. The emittance of these ensembles was compared to the nominal selection in each momentum bin. The overall uncertainty due to beam selection is summarised in table 3. The dominant beam-selection uncertainty is in the selection of particles that successfully pass within the inner 90 mm of the diffuser aperture.

8.2.2 Correlated systematic uncertainties

Some systematic uncertainties are correlated with the total momentum, p. For example, the measured value of p dictates the momentum bin a muon is assigned to for the emittance calculation. The uncertainty on the emittance reconstructed in each bin has been evaluated by allowing the momentum of each muon to fluctuate around its measured value according to a Gaussian distribution of width equal to the measurement uncertainty on p. In table 3 this uncertainty is listed as 'Binning in p'.

A second uncertainty that may be correlated with total momentum is the uncertainty on the reconstructed x, p_x, y, p_y. The effect on the emittance was evaluated using a procedure equivalent to that used to evaluate the uncertainty related to binning in total momentum. This uncertainty is listed as 'Tracker resolution' in table 3.

Systematic uncertainties, correlated with p are primarily due to the differences between the model of the apparatus used in the reconstruction and the hardware actually used in the experiment, of which the most significant component is the magnetic field within the tracking volume. Particle tracks are reconstructed assuming a uniform solenoidal field, with no fringe-field effects. Small non-uniformities in the magnetic field in the tracking volume will result in a disagreement between the true parameters and the reconstructed values. To quantify this effect, six field models (one optimal and five additional models) were used to estimate the deviation in reconstructed emittance from the true value under realistic conditions. Three families of field model were investigated, corresponding to the three key field descriptors: field scale, field alignment, and field uniformity. For each of these descriptors the best known values were used to define the optimal model and the uncertainty in the known values were used to probe the 1σ variations.

8.2.3 Field scale

Hall-probes located on the tracker provided measurements of the magnetic field strength within the tracking volume at known positions. An optimal field model was produced with a scale factor that optimally reproduced the Hall-probe measurements and two additional field models were produced which used scale factors that were one standard deviation above and below the nominal value.

8.2.4 Field alignment

A field-alignment algorithm was developed based on the determination of the orientation of the field with respect to the mechanical axis of the tracker using coaxial tracks with $p_t \approx 0$ [40]. The optimal field model was created such that the simulated alignment is in agreement with the measurements. Two additional models that vary the alignment by one standard deviation were also produced.

8.2.5 Field uniformity

A Comsol [35] model of the field was used to generate the optimal model which includes the field generated by each coil using the 'as-built' parameters and the partial return yoke, which can cause variations in the on axis field by several percent. A simple field model was created using only the individual coil geometries to provide additional information on the effect of field uniformity on the reconstruction. The values for this field were normalised to the Hall-probe measurements as for the other field models. This represents a significant deviation from the COMSOL model, but demonstrates the stability of the reconstruction with respect to changes in field uniformity as the variation in emittance between all proposed field models was small.

For each of the 5 field models, multiple 2000-muon ensembles were generated for each momentum bin. The deviation of the calculated emittance from the true emittance was found for each ensemble. The distribution of the difference between the ensemble emittance and the true emittance was assumed to be Gaussian with mean ε and variance $s^2 = \sigma^2 + \theta^2$, where σ is the theoretical statistical uncertainty and θ is an additional systematic error. The systematic bias for each momentum bin was then calculated as [41]:

$$b = \langle\varepsilon\rangle - \varepsilon_{\text{true}}\,; \tag{6}$$

where $\varepsilon_{\text{true}}$ is the true beam emittance in that momentum bin and $\langle\varepsilon\rangle$ is the mean emittance from the N ensembles. The systematic uncertainty was calculated assuming that the distribution of residuals of ε_i from the mean $\langle\varepsilon\rangle$, satisfies a χ^2 distribution with $N-1$ degrees of freedom:

$$\chi^2_{N-1} = \sum_i^N \frac{(\varepsilon_i - \langle\varepsilon\rangle)^2}{\sigma^2 + \theta^2}\,; \tag{7}$$

and θ was estimated by minimising the expression $(\chi^2_{N-1} - (N-1))^2$.

The uncertainty, θ, was consistent with zero in all momentum bins, whereas the bias, b, was found to be momentum dependent, as shown in figure 12. The bias was estimated from the mean difference between the reconstructed and true emittance values using the optimal field model. The variation in the bias was calculated from the range of values reconstructed for each of the additional field models. The model representing the effects of non-uniformities in the field was considered separately due to the significance of the deviation from the optimal model.

The results show a consistent systematic bias of ≈ -0.015 mm with momentum, p. The absolute variation in the mean values between the models that were used was smaller than the expected statistical fluctuations, demonstrating the stability of the reconstruction across the expected variations in field alignment and scale. The effect of the non-uniformity model was larger but still demonstrates consistent reconstruction in cases where non-physical fields are being used. The biases calculated from the optimal field model were used to the correct the emittance values in the final calculation (Section 8.3).

8.3 Emittance

The measured normalised transverse emittance as a function of p is shown in figure 13. The emittance has been corrected for the systematic bias in table 3. The uncertainties plotted are those summarised in table 3, where the bars represent the statistical uncertainty and the coloured bands the systematic uncertainty. The statistical uncertainty, systematic uncertainty, and systematic biases follow in Section 8. The emittance is approximately flat between $195 \leq p \leq 245$ MeV/c. This is consistent with the expectation from figure 9, where the majority of the beam propagates along the design axis of the experiment. The mean emittance in this region is ≈ 3.7 mm. The emittance of the reconstructed Monte Carlo is consistently lower than that of the data.

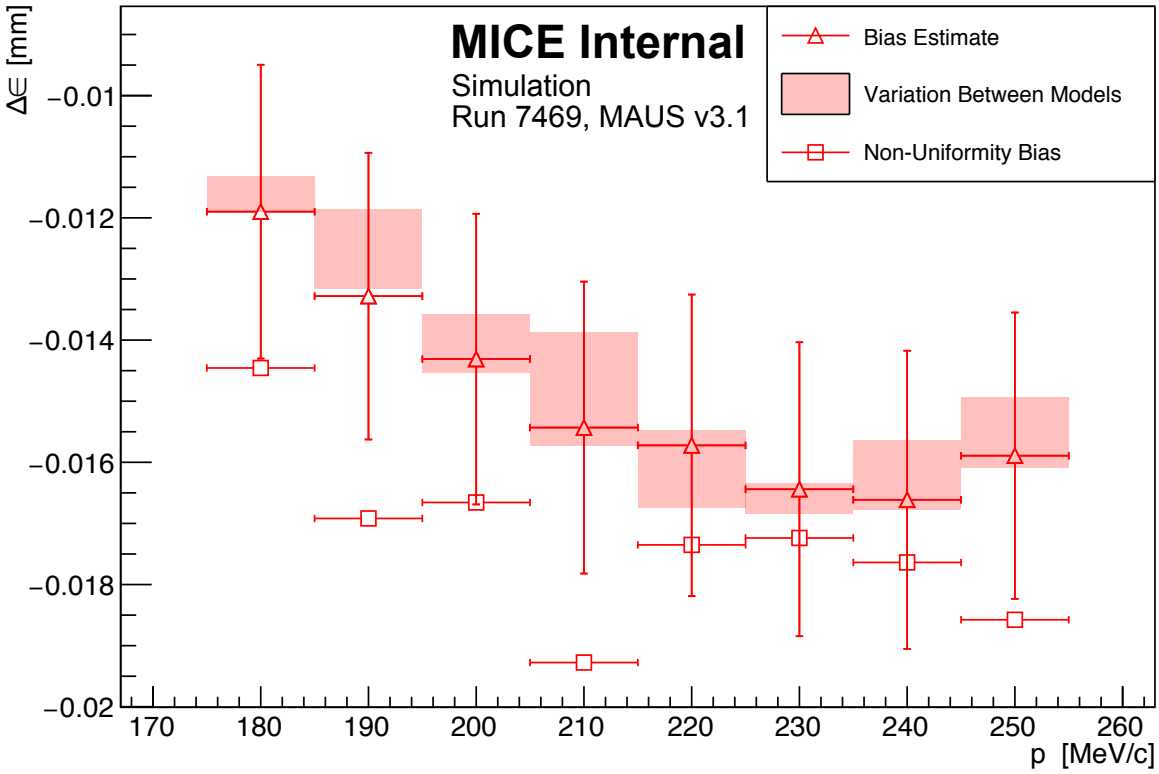

Figure 12: The systematic bias and uncertainty on the reconstructed emittance under different magnetic field model assumptions. The bias estimate includes the shown non-uniformity bias.

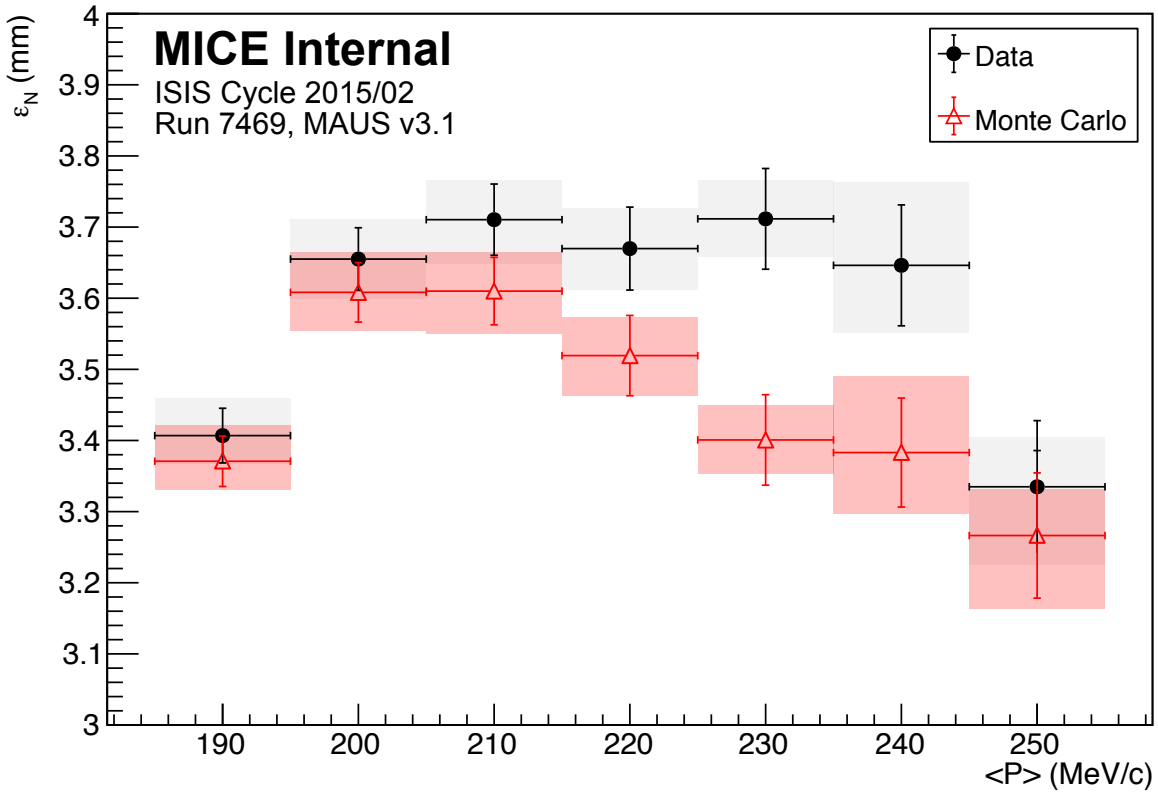

Figure 13: Normalised transverse emittance as a function of momentum, p, for data (black, filled circle) and reconstructed Monte Carlo (red, open triangle). The statistical uncertainty is shown by the error bars and the systematic uncertainty is shown by the shaded bands.

Table 3: Statistical and systematic uncertainties and biases, on the measured emittance as a function of momentum, p.

Source	$\langle p \rangle$ (MeV/c)						
	190	200	210	220	230	240	250
Measured emittance (mm rad)	3.40	3.65	3.69	3.65	3.69	3.62	3.31
Statistical uncertainty	± 0.04	± 0.04	± 0.05	± 0.06	± 0.07	± 0.08	± 0.09
Beam selection:							
Diffuser aperture	$^{+0.05}_{-0.04}$	$^{+0.05}_{-0.05}$	$^{+0.05}_{-0.06}$	$^{+0.05}_{-0.05}$	$^{+0.04}_{-0.04}$	$^{+0.11}_{-0.05}$	$^{+0.04}_{-0.10}$
$\frac{\chi^2}{N_{\mathrm{DOF}}} \leq 4$	$^{+0.01}_{-0.00}$	$^{+0.00}_{-0.00}$	$^{+0.01}_{-0.00}$	$^{+0.00}_{-0.00}$	$^{+0.00}_{-0.00}$	$^{+0.01}_{-0.01}$	$^{+0.01}_{-0.00}$
Muon hypothesis	$^{+0.00}_{-0.00}$	$^{+0.00}_{-0.01}$	$^{+0.01}_{-0.00}$	$^{+0.00}_{-0.00}$	$^{+0.00}_{-0.01}$	$^{+0.01}_{-0.07}$	$^{+0.01}_{-0.00}$
Beam selection (Overall)	$^{+0.05}_{-0.04}$	$^{+0.05}_{-0.05}$	$^{+0.05}_{-0.06}$	$^{+0.05}_{-0.05}$	$^{+0.04}_{-0.04}$	$^{+0.11}_{-0.08}$	$^{+0.04}_{-0.10}$
Binning in p	± 0.02	± 0.02	± 0.02	± 0.03	± 0.03	± 0.04	± 0.05
Magnetic field misalignment and scale:							
Bias	-0.01	-0.01	-0.02	-0.02	-0.02	-0.02	-0.02
Uncertainty	0.00	0.00	0.00	0.00	0.00	0.00	0.00
Tracker resolution	± 0.00	± 0.00	± 0.00	± 0.00	± 0.01	± 0.01	± 0.01
Total systematic uncertainty	$^{+0.05}_{-0.04}$	± 0.06	± 0.06	± 0.06	± 0.05	$^{+0.12}_{-0.09}$	$^{+0.07}_{-0.11}$
Corrected emittance (mm rad)	3.41	3.66	3.71	3.67	3.71	3.65	3.34
Total uncertainty	± 0.06	± 0.07	$^{+0.07}_{-0.08}$	± 0.08	± 0.09	$^{+0.14}_{-0.13}$	$^{+0.12}_{-0.14}$
Total uncertainty (%)	$^{+1.90}_{-1.63}$	$^{+1.96}_{-1.94}$	$^{+2.01}_{-2.15}$	$^{+2.19}_{-2.34}$	$^{+2.40}_{-2.37}$	$^{+3.97}_{-3.49}$	$^{+3.47}_{-4.30}$

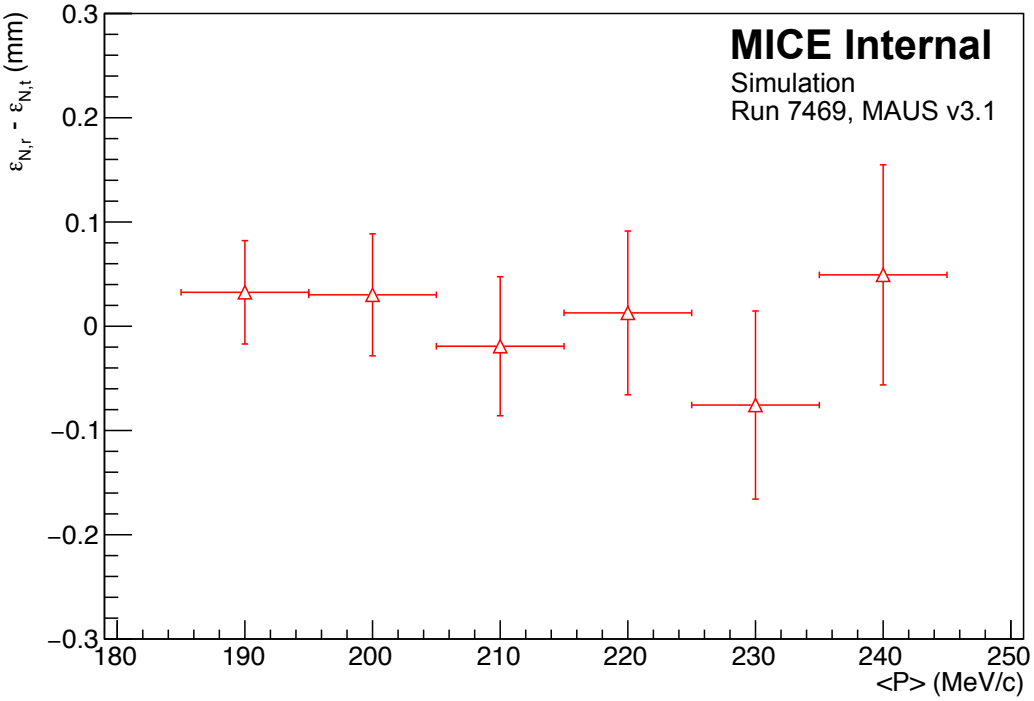

Figure 14: Difference between reconstructed simulated emittance in each 10 MeV/c momentum bin and the true simulated emittance of that bin. Error bars are statistical only, and the residual emittance is approximately flat and consistent with zero within statistical fluctuations.

The difference between (simulated) reconstructed and (simulated) true emittance is shown in figure 14. Each momentum bin includes only those muons that pass all selection criteria (Section 6). If a muon's reconstructed momentum falls within the bin, it is used to calculate the reconstructed emittance of the bin. Similarly, if a particle's true momentum falls within the bin, it is used to calculate the true emittance of the bin. The difference between the reconstructed and true emittance in each bin is consistent with zero within statistical errors.

9 Conclusions

A first measurement of the emittance of the MICE muon beam was made using the upstream scintillating-fibre tracking detector in a 4 T solenoidal field. A total of 24 660 muons survive the selection criteria. The position and momenta of these muons were measured at the reference plane of the upstream tracking detector. The measured muons were binned according to total momentum, p, into $p = 10$ MeV/c ensembles from 185–255 MeV/c to account for dispersion, chromaticity, and scraping in apertures upstream from the tracking detector. The emittance is approximately flat from $195 \leq p \leq 245$ MeV/c with a mean value of ≈ 3.7 mm across this region.

The total uncertainty on this measurement ranged from $^{+1.90}_{-1.63}$ to $^{+3.47}_{-4.30}$%, increasing with total momentum, p. As p increases, the number of muons in the reported ensemble decreases, increasing the statistical uncertainty. At the extremes of the momentum range, a larger proportion of the input beam distribution is scraped on the aperture of the diffuser. This contributes to an increase in systematic uncertainty at the limits of the reported momentum range. The systematic uncertainty introduced by the diffuser aperture highlights the need to study ensembles where the total momentum, p, is close to the design momentum of the beam line.

The technique presented here represents the first precision measurement of normalised transverse emittance on a particle-by-particle basis. This technique will be applied to muon ensembles up- and downstream of a low-Z absorber, such as liquid hydrogen or lithium hydride, to measure emittance change across the absorber.

References

[1] S. Geer, "Neutrino beams from muon storage rings: Characteristics and physics potential," *Phys. Rev.* **D57** (1998) 6989–6997, arXiv:hep-ph/9712290.

[2] M. Apollonio *et al.*, "Oscillation physics with a neutrino factory," hep-ph/0210192.

[3] D. V. Neuffer and R. B. Palmer, "A High-Energy High-Luminosity $\mu^+ - \mu^-$ Collider," *Conf. Proc.* **C940627** (1995) 52–54.

[4] R. B. Palmer, "Muon Colliders," *Rev. Accel. Sci. Tech.* **7** (2014) 137–159.

[5] M. Boscolo, M. Antonelli, O. R. Blanco-Garcia, S. Guiducci, S. Liuzzo, P. Raimondi, and F. Collamati, "Studies of a scheme for Low EMittance Muon Accelerator with production from positrons on target," arXiv:1803.06696 [physics.acc-ph].

[6] S. Y. Lee, *Accelerator Physics (Third Edition)*. World Scientific Publishing Co, 2012.

[7] S. Schröder, R. Klein, N. Boos, M. Gerhard, R. Grieser, G. Huber, A. Karafillidis, M. Krieg, N. Schmidt, T. Kühl, R. Neumann, V. Balykin, M. Grieser, D. Habs, E. Jaeschke, D. Krämer, M. Kristensen, M. Music, W. Petrich, D. Schwalm, P. Sigray, M. Steck, B. Wanner, and A. Wolf, "First laser cooling of relativistic ions in a storage ring," *Phys. Rev. Lett.* **64** (Jun, 1990) 2901–2904. http://link.aps.org/doi/10.1103/PhysRevLett.64.2901.

[8] J. S. Hangst, M. Kristensen, J. S. Nielsen, O. Poulsen, J. P. Schiffer, and P. Shi, "Laser cooling of a stored ion beam to 1 mk," *Phys. Rev. Lett.* **67** (Sep, 1991) 1238–1241. http://link.aps.org/doi/10.1103/PhysRevLett.67.1238.

[9] P. J. Channell, "Laser cooling of heavy ion beams," *Journal of Applied Physics* **52** no. 6, (1981) 3791–3793, http://dx.doi.org/10.1063/1.329218. http://dx.doi.org/10.1063/1.329218.

[10] J. Marriner, "Stochastic cooling overview," *Nucl. Instrum. Meth.* **A532** (2004) 11–18, arXiv:physics/0308044 [physics].

[11] V. V. Parkhomchuk and A. N. Skrinsky, "Electron cooling: 35 years of development," *Physics-Uspekhi* **43** no. 5, (2000) 433–452. http://stacks.iop.org/1063-7869/43/i=5/a=R01.

[12] A. N. Skrinsky and V. V. Parkhomchuk, "Cooling Methods for Beams of Charged Particles. (In Russian)," *Sov. J. Part. Nucl.* **12** (1981) 223–247. [Fiz. Elem. Chast. Atom. Yadra12,557(1981)].

[13] D. Neuffer, "Principles and Applications of Muon Cooling," *Conf.Proc.* **C830811** (1983) 481.

[14] D. Neuffer, "Principles and Applications of Muon Cooling," *Part. Accel.* **14** (1983) 75–90.

[15] The MICE collaboration, "INTERNATIONAL MUON IONIZATION COOLING EXPERIMENT." http://mice.iit.edu.

[16] **ISS Accelerator Working Group** Collaboration, M. Apollonio *et al.*, "Accelerator design concept for future neutrino facilities," *JINST* **4** (2009) P07001, arXiv:0802.4023 [physics.acc-ph].

[17] J. B. Rosenzweig, *Fundamentals of Beam Physics*. Oxford University Press, 2003.

[18] **Mice Collaboration** Collaboration, R. Bertoni *et al.*, "The design and commissioning of the MICE upstream time-of-flight system," *Nucl.Instrum.Meth.* **A615** (2010) 14–26, arXiv:1001.4426 [physics.ins-det].

[19] R. Bertoni, M. Bonesini, A. de Bari, G. Cecchet, Y. Karadzhov, and R. Mazza, "The construction of the MICE TOF2 detector." http://mice.iit.edu/micenotes/public/pdf/MICE0286/MICE0286.pdf, 2010.

[20] L. Cremaldi, D. A. Sanders, P. Sonnek, D. J. Summers, and J. Reidy, Jr, "A Cherenkov Radiation Detector with High Density Aerogels," *IEEE Trans. Nucl. Sci.* **56** (2009) 1475–1478, arXiv:0905.3411 [physics.ins-det].

[21] M. Ellis *et al.*, "The design, construction and performance of the MICE scintillating fibre trackers," *Nucl. Instrum. Meth.* **A659** (2011) 136–153, arXiv:1005.3491 [physics.ins-det].

[22] **MICE collaboration** Collaboration, M. Bogomilov *et al.*, "The MICE Muon Beam on ISIS and the beam-line instrumentation of the Muon Ionization Cooling Experiment," *JINST* **7** (2012) P05009, arXiv:1203.4089 [physics.acc-ph].

[23] F. Ambrosino *et al.*, "Calibration and performances of the KLOE calorimeter," *Nucl. Instrum. Meth.* **A598** (2009) 239–243.

[24] R. Asfandiyarov *et al.*, "The design and construction of the MICE Electron-Muon Ranger," *JINST* **11** no. 10, (2016) T10007, arXiv:1607.04955 [physics.ins-det].

[25] C. N. Booth *et al.*, "The design, construction and performance of the MICE target," *JINST* **8** (2013) P03006, arXiv:1211.6343 [physics.ins-det].

[26] C. N. Booth *et al.*, "The design and performance of an improved target for MICE," *JINST* **11** no. 05, (2016) P05006, arXiv:1603.07143 [physics.ins-det].

[27] **MICE** Collaboration, D. Adams *et al.*, "Characterisation of the muon beams for the Muon Ionisation Cooling Experiment," *Eur. Phys. J.* **C73** no. 10, (2013) 2582, arXiv:1306.1509 [physics.acc-ph].

[28] A. Dobbs, C. Hunt, K. Long, E. Santos, M. A. Uchida, P. Kyberd, C. Heidt, S. Blot, and E. Overton, "The reconstruction software for the MICE scintillating fibre trackers," *JINST* **11** no. 12, (2016) T12001, arXiv:1610.05161 [physics.ins-det].

[29] S. Blot, "Proton Contamination Studies in the MICE Muon Beam Line," *Proceedings 2nd International Particle Accelerator Conference (IPAC 11) 4-9 September 2011, San Sebastian, Spain* (2011) .

[30] T. Roberts *et al.*, "G4beamline; a "Swiss Army Knife" for Geant4, optimized for simulating beamlines." http://www.muonsinc.com/muons3/tiki-index.php?page=G4beamline.

[31] A. Dobbs *et al.*, "The reconstruction software for the mice scintillating fibre trackers." http://mice.iit.edu/micenotes/public/pdf/MICE451/MICE451.pdf, 2014.

[32] **GEANT4** Collaboration, S. Agostinelli *et al.*, "Geant4: A simulation toolkit," *Nuclear Instruments and Methods in Physics Research A* **506** (2003) 250–303.

[33] J. Allison *et al.*, "Geant4 developments and applications," *IEEE Trans. Nucl. Sci.* **53** (2006) 270–278.

[34] R. Brun and F. Rademakers, "ROOT: An object oriented data analysis framework," *Nucl. Instrum. Meth.* **A389** (1997) 81–86.

[35] HTTP://WWW.COMSOL.COM/.

[36] **MICE** Collaboration, M. Bogomilov *et al.*, "Pion contamination in the MICE muon beam," *JINST* **11** no. 03, (2016) P03001, arXiv:1511.00556 [physics.ins-det].

[37] J. Cobb, "Statistical Errors on Emittance Measurements." http://mice.iit.edu/micenotes/public/pdf/MICE341/MICE268.pdf, 2009.

[38] J. Cobb, "Statistical Errors on Emittance and Optical Functions." http://mice.iit.edu/micenotes/public/pdf/MICE341/MICE341.pdf, 2011.

[39] J. H. Cobb, "Statistical errors on emittance." Unpublished., 2015.

[40] C. Hunt, "Mice note in preparation,".

[41] L. Lyons, "On estimating systematic errors from repeated measurements," *Journal of Physics A: Mathematical and General* **25** no. 7, (1992) 1967. http://stacks.iop.org/0305-4470/25/i=7/a=035.